RSC Advances

PAPER

View Article Online
View Journal | View Issue

Cite this: *RSC Adv.*, 2023, **13**, 7673

Ultrafine Pt nanoparticles anchored on core–shell structured zeolite–carbon for efficient catalysis of hydrogen generation†

Yue-Wei Wei,[abd] Guang Yang,[d] Xi-Xi Xu,[d] Yan-Yan Liu,[e] Bao-Jun Li,*[c] Yong-Zhao Wang*[ab] and Yong-Xiang Zhao*[ab]

Ammonia borane (AB) is a potential hydrogen storage material with high-efficiency hydrolytic dehydrogenation under a suitable catalyst. Noble metal catalysts have drawn a lot of attention. In this study, a carbon-coated zeolite was obtained by calcination at high temperatures using glucose as a carbon source. Pt nanoparticles were fixed on a core–shell composite support by a simple chemical reduction method. A series of catalysts were prepared with different synthesis parameters. The results show that PSC-2 has excellent catalytic performance for hydrolytic dehydrogenation of AB in alkaline solution at room temperature, and the turnover frequency (TOF) is 593 min^{-1}. The excellent catalytic performance is attributed to the carbon layer on the zeolite surface which inhibits the aggregation or deformation of metals in the catalytic reaction. The metal-support interaction activates the water and accelerates the rate-limiting step of hydrolysis. The activation energy (E_a = 44 kJ mol^{-1}) was calculated based on the reaction temperature. In addition, the kinetics of AB hydrolysis was studied, and the effects of catalyst concentration, AB concentration and NaOH concentration on AB hydrolysis rate were further investigated. The high-efficiency catalyst prepared in this work provides a new strategy for the development of chemical hydrogen production in the field of catalysis.

Received 17th January 2023
Accepted 7th February 2023

DOI: 10.1039/d3ra00358b

rsc.li/rsc-advances

1. Introduction

Increasing energy consumption and environmental degradation make the development of clean energy particularly important. To meet the energy demand, people must develop new alternative energy sources. Hydrogen is an excellent energy carrier that is environmentally friendly after combustion and has a higher energy density than fossil fuels. It is widely regarded as one of the most promising clean energy sources.[1–5] However, the efficient storage and controlled release of hydrogen limit the practical application of hydrogen energy. Therefore, safe and reliable storage of hydrogen under environmental conditions is widely studied.[6–9] Hydrogen can be stored chemically in some materials, such as metal hydrides,[10] hydrazine hydrate,[11] borohydrides,[12,13] and ammonia borane (AB).[14,15] The advantages of high hydrogen content (19.6 wt%), stability and non-toxicity make AB a potential hydrogen storage material.[16–18] AB is stable in aqueous solution for a long time, but it has good thermodynamics for hydrolysis and release of hydrogen. Each mole of AB can release 3 mol of H_2, as shown in reaction (1).

$$NH_3BH_3 + 2H_2O \rightarrow NH_4^+ + BO_2^- + 3H_2\uparrow \quad (1)$$

A safe, effective, and useful hydrogen production technique, AB's hydrolytic hydrogen production can be controlled by the catalyst and benefits from mild reaction conditions and no CO.[19] Owing to the strong hydrolysis resistance of AB aqueous solution under environmental conditions, the suitable catalyst is needed to accelerate hydrolysis reaction. A suitable catalyst is key to the hydrolysis reaction of AB.[20,21] At present, many catalysts for hydrolytic dehydrogenation of AB have been extensively studied, including transition metal catalysts such as Pt,[22,23] Rh,[24,25] Ru,[26,27] Pd,[28,29] Co,[30,31] and Ni.[32,33] Although noble metals have a high price and few resources, they have characteristics of long life and high activity. Previous studies have shown that catalysts containing noble metals have higher catalytic activity and lower activation energy.[34–36] However, to realize the practical application of AB

[a]School of Chemistry and Chemical Engineering, Shanxi University, Taiyuan 030006, China. E-mail: catalyst@sxu.edu.cn; yxzhao@sxu.edu.cn
[b]Engineering Research Center of Ministry of Education for Fine Chemicals, Shanxi University, Taiyuan 030006, China
[c]Research Center of Green Catalysis, College of Chemistry, Zhengzhou University, Zhengzhou 450001, China. E-mail: lbjfcl@zzu.edu.cn
[d]Tobacco College of Henan Agricultural University, Zhengzhou 450002, China
[e]College of Science, Henan Agricultural University, Zhengzhou 450002, China

† Electronic supplementary information (ESI) available: Some SEM, XPS, and comparison of catalytic performance. See DOI: https://doi.org/10.1039/d3ra00358b

in hydrogen energy, it is still a great challenge to develop efficient and stable catalysts. Pt-based catalysts have attracted much attention as excellent catalysts in various reactions.[37,38] Highly scattered Pt nanoparticles (NPs) have been prepared using a variety of supports to increase the number of atoms that are exposed to the catalyst surface and hence enhance the catalytic efficiency of the catalyst.[39,40] Suitable support is very important for the stability and activity of metal-based catalysts. The catalysts show excellent catalytic activity because the support materials with large specific surface areas and suitable porosity can evenly spread metal NPs and provide a synergistic effect.[41–46] Shen *et al.* reported engineering bimodal oxygen vacancies and Pt to boost the activity toward water dissociation.[47] A bimodal oxygen vacancy (VO) catalysis strategy is adopted to boost the efficient water dissociation on Pt nanoparticles. The single facet-exposed TiO_2 surface and NiO_x nanocluster possess two modes of VO different from each other. In ammonia borane hydrolysis, the highest catalytic activity among Pt-based materials is achieved with a turnover frequency of 618 min^{-1} under alkaline-free conditions at 298 K. Zeolite is widely used as a catalyst or carrier material in the large-scale petroleum industry.[48,49] However, the metal NPs on the catalyst surface tend to aggregate and form larger particles. The porous structure of carbon materials can effectively prevent the aggregation of metal NPs and increase their active sites. Carbon-based materials are widely used as supports.[50,51] Liu *et al.* reported a NiRu alloy anchored on the surface of nitrogen-doped carbon-coated titanium dioxide showed the highest catalytic activity (2.51 × 105 mL min^{-1} $g_{Ru}{}^{-1}$) for NH_3BH_3 hydrolysis at 298 K. The unprecedented activity is beyond previous reports.[52]

In this paper, a carbon–zeolite support was prepared by calcination at high temperatures with glucose as carbon source. The resulting composite support was impregnated in the Pt precursor solution. By a simple chemical reduction method, the Pt NPs were fixed on composite support with a core–shell structure, and the supported Pt-based catalyst was obtained. A series of catalysts (PSC-*x*) were prepared with different synthesis parameters. The results show that PSC-2 has excellent catalytic performance for hydrolytic dehydrogenation of AB at room temperature, and the turnover frequency (TOF) is 593 min^{-1}. In addition, the catalytic mechanism of AB hydrolysis was proposed. The high catalytic activity is attributed to the metal-support interaction and the inhibition of metal aggregation or deformation by the carbon layer on the zeolite surface. According to the reaction temperature, the activation energy (E_a = 44 kJ mol^{-1}) was obtained. The interaction of Pt–zeolite speeds up the rate-limiting step of water dissociation in the hydrolysis reaction. This study provides a new opportunity for the industrial application of noble metal nanocatalysts in the field of hydrogen energy.

2. Experimental section

2.1 Preparation of materials

2.1.1 Preparation of support. A certain amount of glucose was dissolved in 100 mL water and stirred for 10 min. Then 5 g of zeolite (S-1) was added and oscillated in the ultrasonic instrument for 10 min. The solution was moved to the water bath and stirred for 1 h to make the zeolite evenly dispersed. The temperature of the water was then raised to 90 °C so that the water in the solution rapidly evaporated. After the solution is completely dried, the white product was ground into a powder. Then it was transferred to the vacuum tube furnace for calcination. Under nitrogen protection, it was heated to 600 °C at the rate of 3 °C min^{-1} and kept for 1 h. Black powder was obtained after calcination, which was denoted as SC-*x*. The amount of glucose was 0, 0.8, 1.2, 1.6, and 2.0 g, respectively, and recorded as SC-*x* (x = 0, 1, 2, 3, 4).

2.1.2 Preparation of catalyst. Chlorplatinic acid (H_2PtCl_6, 1 mL, 0.01 g mL^{-1}) was added into 60 mL water, and after stirring well, 1 g support (SC-*x*) was added. The solution was placed in the ultrasonic instrument for 30 min oscillation and then stirred for 1 h. Quickly add 3 mL sodium borohydride solution (0.1 M) and continue to stir for 2 h. The solution was processed by centrifugation (4000 rpm, 5 min), rinsed 3 times with deionized water, and then dried in an oven at 80 °C. Catalysts prepared with different supports were recorded as PSC-*x* (x = 0, 1, 2, 3, 4). The theoretical content of Pt in the prepared catalyst is 1 wt%.

2.2 Characterization

The crystalline phases of the prepared catalysts were characterized by X-ray powder diffraction (XRD, Bruker/D8-Advance, Cu Kα, λ = 1.5418 Å) in the 2θ range from 5° to 80°. The Raman spectrum was recorded on a HORIBA LabRAM HR Evolution Raman Spectrometer (Horiba Scientific, Japan) with excitation from the 532 nm line of the Ar-ion laser at a power of about 5 mW. The morphology of catalysts was studied by using transmission electron microscope (HRTEM, FEI Tecnai G2 F20 S-TWIN electron microscope, operating at 200 kV) and scanning electron microscopy (SEM, ZEISS sigma500, Germany). The metal content was determined by inductively coupled plasma optical emission spectrometer (ICP-OES, Agilent-5110, USA). X-ray photoelectron spectroscopy (XPS) was recorded on a Thermo ESCALAB 250 electron spectrometer with an Al Kα = 1486.6 eV excitation source, and the binding energy was calibrated by reference to the C 1s peak (284.8 eV) to reduce the charge effect of the sample. The N_2 sorption isotherms were measured on surface area and pore size analyzer (MicromeriticTristar 3000, USA) at 77 K. The specific surface areas (S_{BET}) of materials were calculated by the multi-point Brunauer–Emmett–Teller (BET) method. The pore size distribution was evaluated by the Barrett–Joyner–Halenda (BJH).

The hydrogen production from AB hydrolysis was monitored by the water displacement method. The catalyst (20 mg) was added to a 25 mL flask, and the flask was placed in a magnetic stirring water bath at a constant temperature of 25 °C. The speed of the stirring device is controlled at 500 rpm. An upside-down measuring cylinder filled with water is used to monitor the volume of hydrogen. A mixture of AB (84 mg) and NaOH (1 M, 10 mL) is then quickly injected into the flask. Bubbles can be observed in the cylinder. Record the time every

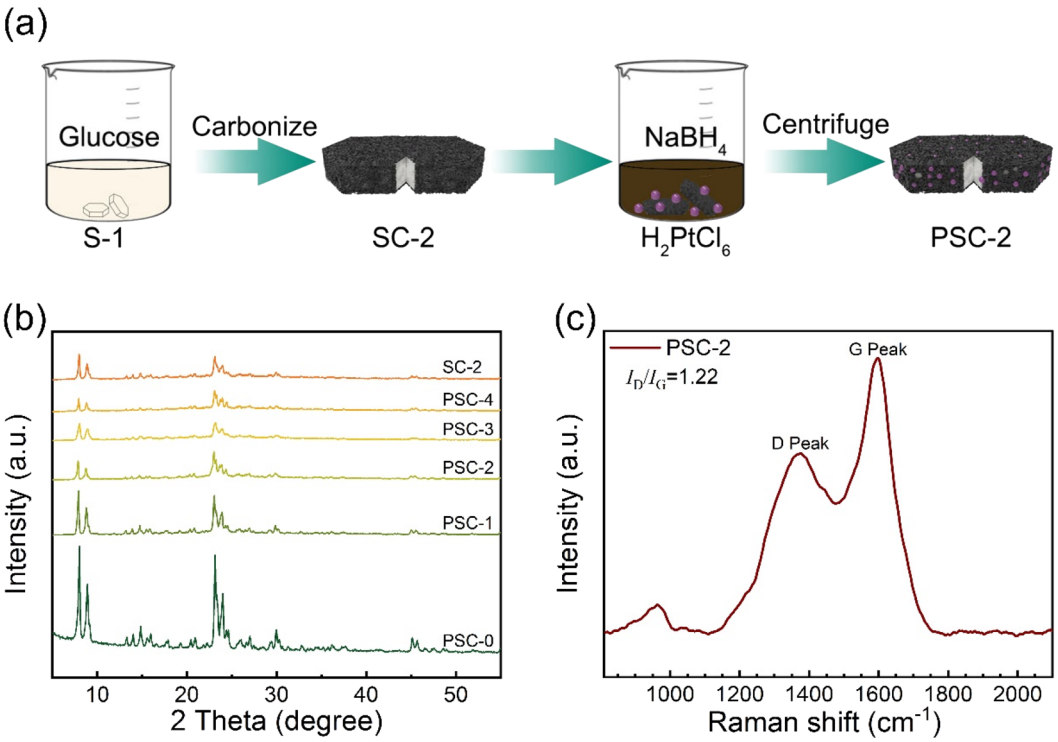

Fig. 1 (a) The preparation process of PSC-2, (b) XRD patterns of catalysts and support, (c) Raman spectra of PSC-2.

10 mL. According to the obtained data (at 80 mL), the TOF value of the catalyst was calculated according to the following formula:

$$\mathrm{TOF} = \frac{n_{\mathrm{H_2}}}{n_{\mathrm{Pt}} \cdot t} \quad (2)$$

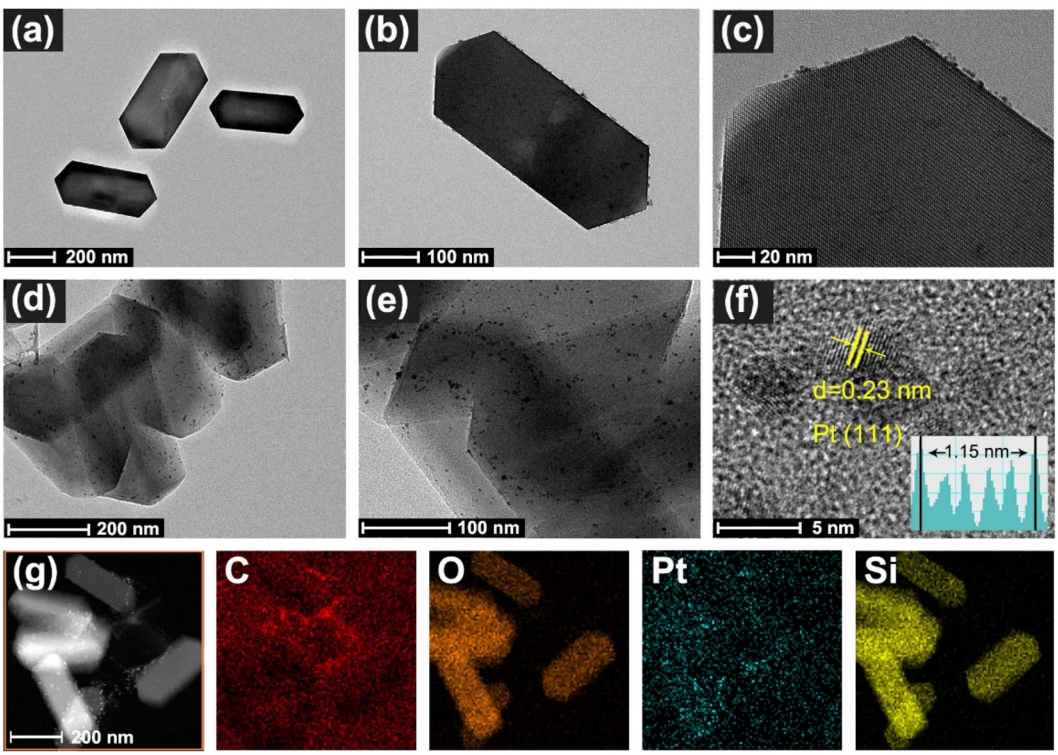

Fig. 2 (a–c) TEM and HRTEM images of PSC-0, (d–f) TEM and HRTEM images of PSC-2, (g) high-angle annular dark field-scanning transmission electron microscopy (HAADF-STEM) image and corresponding EDX-STEM element mapping images of PSC-2.

TOF is the turnover frequency, n_{H_2} is the number of moles of hydrogen, n_{Pt} is the number of moles of platinum, and t is the time of hydrogen to 80 mL, in minutes.

3. Results and discussion

Fig. 1a shows the preparation process of the catalyst. The supported catalyst in this study was synthesized by a simple *in situ* reduction method. Firstly, zeolite and glucose are mixed thoroughly, and then carbon–zeolite support is formed after high-temperature calcination. The Pt metal precursor was reduced by sodium borohydride to form metal nanoparticles, which were effectively anchored to support. Carbon materials effectively limit the aggregation of Pt NPs. The interaction between metal and support enhances the catalytic activity of the catalyst.

Phase analysis of support and catalyst was performed by X-ray powder diffraction (Fig. 1b). The results show that the broad peak at about 23.6° is identified as amorphous carbon. The diffraction peak between 8°–30° is assigned to the standard peak position of S-1 (JCPDS Card No. 44-0696). The intensity and position of the diffraction peak of support do not shift. This indicated that the structure of support remained intact without loss of skeleton lattice and crystallinity after the Pt precursor was reduced during catalyst synthesis. However, the characteristic peak of Pt NPs was not found, which was attributed to the small particle size and a low load of Pt NPs in the catalyst. The catalyst was tested and analyzed by Raman spectroscopy (Fig. 1c). Two distinct peaks in the figure are attributed to the best catalyst (PSC-2). The D and G peaks are Raman characteristic peaks of C atom crystals. Peak D near 1381 cm^{-1} represents a defect in the lattice of C atoms. Peak G near 1594 cm^{-1} represents the in-plane stretching vibration of sp^2 hybridization of the C atom.[53,54] The intensity ratio (I_D/I_G) of peak D to peak G is 1.22, indicating that the C-atom crystal has more defects. The integrated area data of D and G peak are shown in Table S1 of ESI.†

The morphology and structure of the catalyst were observed by TEM. The TEM image of PSC-0 is shown in Fig. 2a–c, showing slight aggregation of metal nanoparticles on the catalyst surface. Fig. 2d–f is attributed to PSC-2. It can be observed that S-1 is coated with carbon, and Pt NPs are uniformly distributed on the catalyst surface. Fig. S1† shows the scanning electron microscope image of PSC-2. The results show that the porous structure of support can effectively inhibit the aggregation of metal particles, thus improving the catalytic performance.[55] As can be seen from Fig. 2f, the particle size of Pt is between 3–5 nm. The crystal lattice with a spacing of 0.23 nm is attributed to the (111) face of Pt (JCPDS No. 04-0802). In addition, Fig. 2g

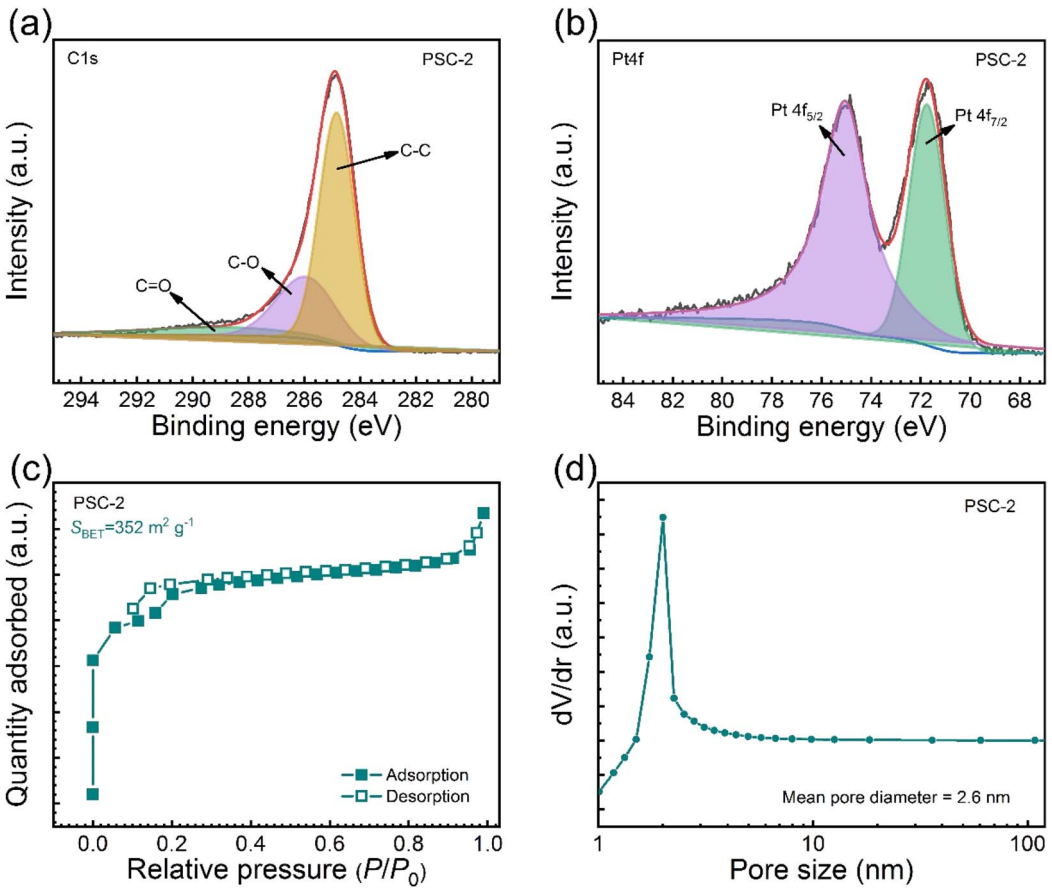

Fig. 3 (a and b) XPS spectra of PSC-2, (c) nitrogen adsorption and desorption isotherms of PSC-2, and (d) pore size distributions of PSC-2 calculated by BJH method.

shows a high-angle annular dark field-scanning transmission electron microscope (HAADF-STEM) image of PSC-2. The elements C, O, Pt, and Si were identified by element mapping, and Pt was uniformly distributed on the catalyst surface. The content of Pt in the catalyst was measured by ICP-OES (Table S2†).

The chemical composition and valence states of PSC-2 were analyzed by X-ray photoelectron spectroscopy (XPS). The spectra in Fig. S2† identify Pt (75 eV), C (287 eV), Si (103 eV), and O (557 eV) elements in the catalyst. This is consistent with the results in EDX. Fig. 3a shows the C 1s spectrum of PSC-2, and the peaks at 284.8, 285.9, and 288.9 eV are attributed to C–C, C–O, and C=O, respectively.[56] Fig. 3b shows the spectrum of Pt 4f. The Pt element mainly exists in the metallic form of Pt(0), and the peaks at 75.0 and 71.7 eV are attributed to Pt $4f_{5/2}$ and Pt $4f_{7/2}$, respectively.[57] The results show that the binding energy of Pt is lower than reported, and the introduction of SC makes electron transfer to surface Pt atoms easier.[58] The reduction in binding energy is attributed to the electron-rich Pt. The electron-rich metal surface promotes the activation of H_2O, thus increasing the activity of the catalyst. Fig. S3† shows the O 1s spectrum of PSC-2. The peak value at 534.0 eV corresponds to oxygen atoms in SiO_2. Fig. S4† shows the Si 2p spectrum of PSC-2, and the peak at 104.6 eV is attributed to Si.

Fig. 3c shows the N_2 adsorption–desorption test. Both support and catalyst show type I isotherms and type H4 hysteresis loops.[59,60] The specific surface areas were 369 $m^2\ g^{-1}$ and 352 $m^2\ g^{-1}$, respectively. The reduction of specific surface area was attributed to Pt loading on the catalyst surface occupying part of the pore. As shown in Fig. 3d, the aperture distribution was analyzed using the BJH model (Barrett–Joiner–Halenda). The results show that the support and catalyst are abundant in micropores and mesoporous. The porous structure can limit the aggregation of metal particles, thus improving the activity of the catalyst.

Suitable support is crucial to the catalyst. A series of catalysts were prepared by changing the parameters of glucose content in the process of catalyst preparation. In addition, S-1 or SC is used as a catalyst to catalyze the hydrolysis of AB, and no reaction occurred within 2 h. The results show that S-1 and SC have no catalytic activity for AB hydrolysis under the same conditions, and Pt is the key for AB hydrolysis. Under environmental conditions, different catalysts are used to catalyze AB hydrolysis to produce hydrogen, and the results are shown in Fig. 4a. The TOF values of different catalysts are obtained by calculation. It can be observed from Fig. 4b that PSC-0 exhibits poor catalytic activity, which is attributed to the lack of carbon protection on the surface of the catalyst, leading to the aggregation of metal particles. However, catalyst activity increased significantly when

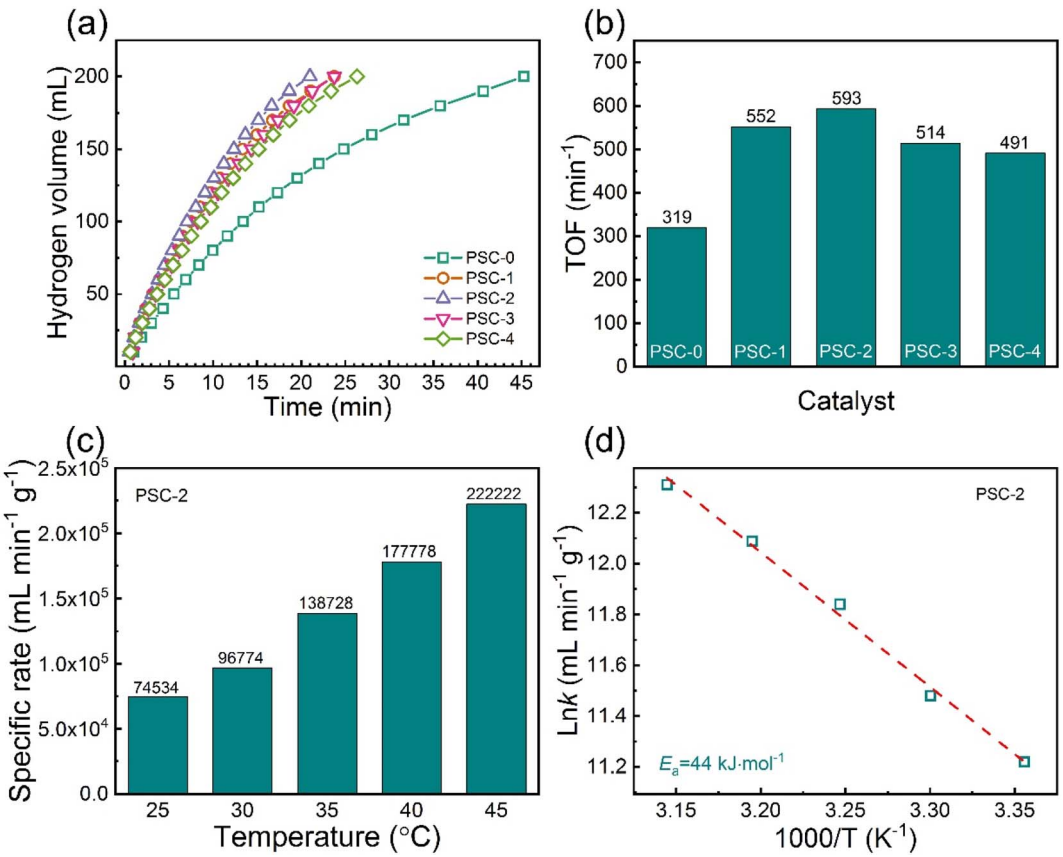

Fig. 4 (a) Hydrogen generation catalyzed by various catalysts at 298 K, (b) TOF values of various catalysts, (c) hydrogen production rates of PSC-2 at different temperatures, (d) Arrhenius plot for PSC-2 hydrolysis of AB under different temperatures.

the zeolite is coated with carbon. Protection of carbon can effectively limit the aggregation of metal particles, and the performance of the catalyst is improved. By adjusting the carbon content, catalyst activity is affected. The addition of excess carbon in the preparation process resulted in a decrease in catalytic activity, possibly owing to the limited interaction of S-1 with Pt NPs. The results show that SC-2 is the best catalyst support, and PSC-2 has excellent catalytic activity with a TOF of 593 min^{-1}.

The catalytic hydrogen production results of PSC-2 at different reaction temperatures (25–45 °C) are shown in Fig. 4c. The rate of hydrogen production increases with increasing temperature, which is attributed to the fact that high temperature increases the activity of water molecules and accelerates the rate-limiting step of the hydrolysis reaction.

Within the temperature range of 298–318 K, the Arrhenius curve of $\ln k$ and the inverse of absolute temperature ($1/T$) is a straight line (Fig. 4d). According to the slope, the activation energy of PSC-2 is 44 kJ mol^{-1}, which is lower than that of most reported metal-based catalysts. PSC-2 is used as a catalyst in subsequent kinetic studies.

In addition, the kinetics of the catalyst is explored. The influence of different AB concentrations on catalyst activity is explored, as shown in Fig. 5a. The results show that amount of hydrogen varies with AB concentration (only 200 mL of data). A line with a slope of 0.16 is fitted between the catalytic rate and AB concentration (Fig. S5†), indicating that AB hydrolysis is a quasi-zero-order reaction with respect to AB concentration.[61] Under the same conditions, different catalyst dosages (5, 10, 20, and 30 mg) are used in the experiment, as shown in Fig. 5b. The catalytic activity is positively correlated with the content of the catalyst, and the hydrolysis rate of AB is increased with the increase of active component. A line with a slope of 1.2 is fitted according to the catalytic rate and catalyst amount (Fig. S6†), indicating that AB hydrolysis is a first-order reaction with regard to catalyst amount. The rate of hydrolysis of AB is accelerated by NaOH. Therefore, the influence of different NaOH concentrations on AB hydrolysis is explored (Fig. 5c). In the initial stage, the catalytic rate increases with the increase of NaOH. The improvement of the catalytic rate is attributed to the coordination of OH^- ions with the metal surface, which makes the metal surface more electron-rich and promotes the activation of H_2O.[62] AB is difficult to hydrolyze in an aqueous solution of NaOH. NaOH is considered a cocatalyst. However, excessive NaOH has an adverse effect on the reaction device and catalyst. Excessive OH^- coordination may occupy the active site on the catalyst surface, resulting in decreased activity. $NaBH_4$ is one of the most widely studied hydrogen storage materials.[63,64] Therefore, PSC-2 is used as a catalyst for hydrolysis of $NaBH_4$ to produce hydrogen (Fig. 5d). The final TOF value is only

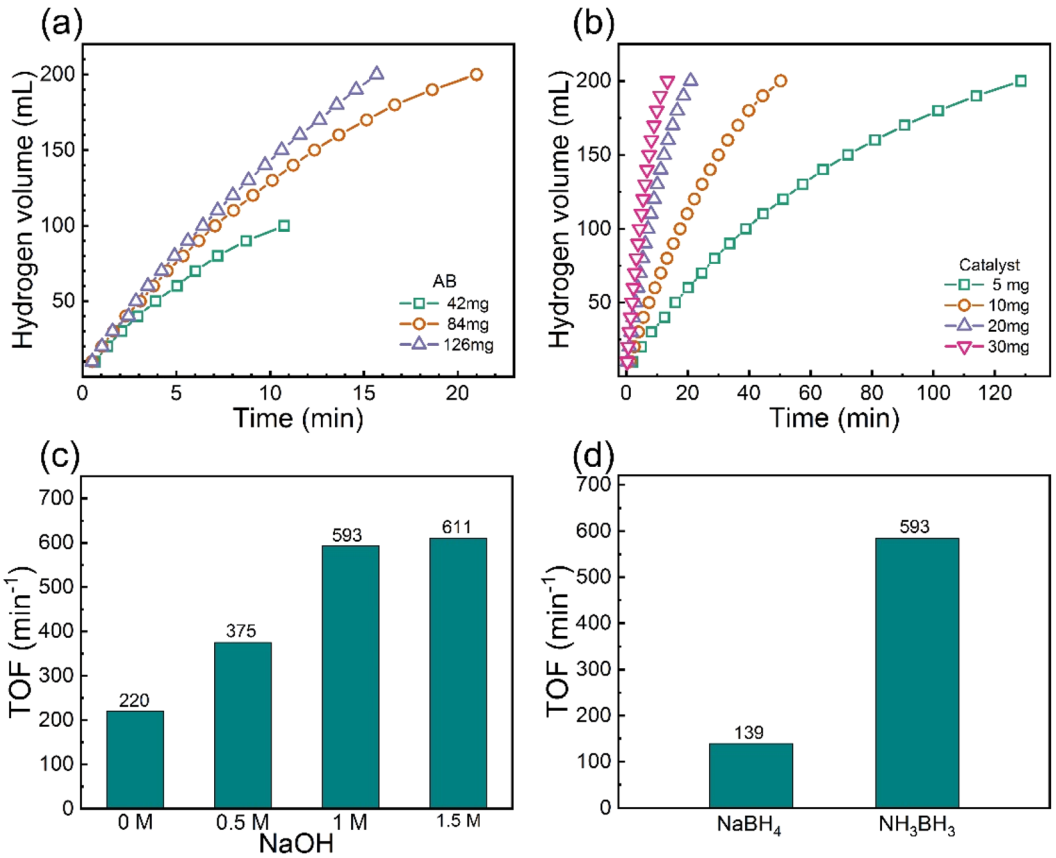

Fig. 5 (a) Hydrolysis rate at different AB concentrations, (b) catalytic hydrogen production with different PSC-2 concentrations, (c) hydrogen generation from the hydrolysis of AB with different NaOH concentrations, and (d) hydrogen production of $NaBH_4$.

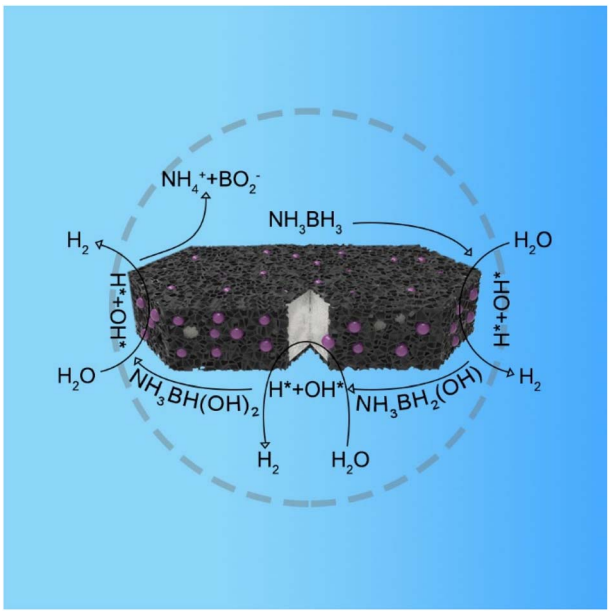

Fig. 6 Diagram of the catalytic mechanism of hydrogen generation of NH_3BH_3.

139 min^{-1}. The results show that PSC-2 has catalytic activity for $NaBH_4$ but has the best catalytic effect for AB.

The mechanism of catalytic hydrolysis of AB by PSC-2 is proposed (Fig. 6). The hydrolysis of AB occurs on the surface of the catalyst.[65–67]

First, H_2O and NH_3BH_3 molecules are activated by electron-rich Pt NPs. H* and OH* are formed by breaking the O–H bond in H_2O. Similarly, NH_3BH_3 is activated causing the B–H bond to break, forming $NH_3BH_2^*$ and H*. Two H* adsorbs form an H_2 molecule and dissociate from the catalyst surface. The OH* attacks $NH_3BH_2^*$ to form NH_3BH_2OH* through a reduction–oxidation step. Second, another H_2O molecule and NH_3BH_2OH* are activated again, and two H* form an H_2 molecule in the same way and dissociate from the catalyst surface. An H_2O molecule is released owing to $NH_3BH(OH)_2^*$ instability formed by OH* and NH_3BHOH*. Subsequently, an H_2 molecule is formed again owing to the B–H bond in NH_3BHO* and the O–H bond in H_2O breaking. Eventually, OH* and NH_3BO* form NH_4^+ and BO_2^-, which is attributed to the attraction of NH_3^* to H. The interaction between S-1 and Pt makes H_2O more easily dissociated and speeds up the rate-limiting step of AB hydrolysis. Therefore, the catalytic performance of PSC-2 is among the top Pt-based catalysts.

4. Conclusions

In summary, carbon–zeolite supports with core–shell structures are prepared using glucose as a carbon source. A series of Pt-based catalysts with different carbon content is obtained. The results show that PSC-2 exhibits excellent catalytic activity (TOF = 593 min^{-1}) for AB hydrolysis under the condition of 298 K alkaline solution. This is attributed to the metal-support interaction between Pt and zeolite which effectively promotes the activation of H_2O and improves the performance of the catalyst. The protection of carbon limits the aggregation of metal particles and increases the exposure of the active site. The apparent activation energy of PSC-2 is determined as E_a = 44 kJ mol^{-1} based on kinetic studies. The electron transfer of metal-carrier interaction is affected by carbon content. PSC-2 is an efficient Pt-based catalyst whose excellent catalytic performance provides a new strategy in the field of catalysis. This work will advance the development of hydrogen energy.

Conflicts of interest

The authors declare no competing financial interests.

Acknowledgements

This study was financially supported by the National Natural Science Foundation of China (No. 22279118, 31901272, U1204203, and 21401168) and the Key Projects of Shanxi Coal-based Low Carbon Joint Fund (No. U1710221).

References

1 I. P. Jain, *Int. J. Hydrogen Energy*, 2009, **34**, 7368–7378.
2 I. Staffell, D. Scamman, A. V. Abad, P. Balcombe, P. E. Dodds, P. Ekins, N. Shah and K. R. Ward, *Energy Environ. Sci.*, 2019, **12**, 463–491.
3 A. Zuettel, A. Remhof, A. Borgschulte and O. Friedrichs, *Philos. Trans. R. Soc., A*, 2010, **368**, 3329–3342.
4 Z. X. Yang, X. G. Li, Q. L. Yao, Z. H. Lu, N. Zhang, J. Xia, K. Yang, Y. Q. Wang, K. Zhang, H. Z. Liu, L. T. Zhang, H. J. Lin, Q. J. Zhou, F. Wang, Z. M. Yu and J. M. Ma, *Rare Met.*, 2022, **41**, 3251–3267.
5 M. Balat, *Int. J. Hydrogen Energy*, 2008, **33**, 4013–4029.
6 C. D. Mboyi, D. Poinsot, J. Roger, K. Fajerwerg, M. L. Kahn and J.-C. Hierso, *Small*, 2021, **17**, 2102759.
7 C. G. Lang, Y. Jia and X. D. Yao, *Energy Storage Mater.*, 2020, **26**, 290–312.
8 P. Jena, *J. Phys. Chem. Lett.*, 2011, **2**, 206–211.
9 A. M. Abdalla, S. Hossain, O. B. Nisfindy, A. T. Azad, M. Dawood and A. K. Azad, *Energy Convers. Manage.*, 2018, **165**, 602–627.
10 Y. F. Liu, K. Zhong, M. X. Gao, J. H. Wang, H. G. Pan and Q. D. Wang, *Chem. Mater.*, 2008, **20**, 3521–3527.
11 S. K. Singh, X.-B. Zhang and Q. Xu, *J. Am. Chem. Soc.*, 2009, **131**, 9894–9895.
12 L. H. Yao, X. G. Li, W. F. Peng, Q. L. Yao, J. H. Xia and Z. H. Lu, *Inorg. Chem. Front.*, 2021, **8**, 1056–1065.
13 Y. Y. Liu, J. Zhang, X. J. Zhang, B. J. Li, X. Y. Wang, H. Q. Cao, D. Wei, Z. F. Zhou and A. K. Cheetham, *J. Mater. Chem. A*, 2016, **4**, 4280–4287.
14 R. F. Shen, Y. Y. Liu, H. Wen, T. Liu, Z. K. Peng, X. L. Wu, X. G. Ge, S. Mehdi, H. Q. Cao, E. J. Liang, J. C. Jiang and B. J. Li, *Appl. Catal., B*, 2022, **306**, 121100.

15 H. H. Zhang, K. Zhang, S. Ashraf, Y. P. Fan, S. Y. Guan, X. L. Wu, Y. S. Liu, B. Z. Liu and B. J. Li, *Energy Environ. Mater.*, 2021, **6**, e12273.
16 U. Sanyal, U. B. Demirci, B. R. Jagirdar and P. Miele, *ChemSusChem*, 2011, **4**, 1731–1739.
17 S. Akbayrak and S. Özkar, *Int. J. Hydrogen Energy*, 2018, **43**, 18592–18606.
18 H. L. Jiang and Q. Xu, *Catal. Today*, 2011, **170**, 56–63.
19 C. L. Wang and D. Astruc, *Chem. Soc. Rev.*, 2021, **50**, 3437–3484.
20 C. Yüksel Alpaydın, S. K. Gülbay and C. Ozgur Colpan, *Int. J. Hydrogen Energy*, 2020, **45**, 3414–3434.
21 Q. M. Sun, N. Wang, Q. Xu and J. H. Yu, *Adv. Mater.*, 2020, **32**, 2001818.
22 W. Y. Chen, W. Z. Zheng, J. B. Cao, W. Z. Fu, G. Qian, D. Chen, X. G. Zhou and X. Z. Duan, *ACS Catal.*, 2020, **10**, 11417–11429.
23 M. Morishita, A. Nozaki, H. Yamamoto, N. Fukumuro, M. Mori, K. Araki, F. Sakamoto, A. Nakamura and H. Yanagita, *RSC Adv.*, 2021, **11**, 14063–14070.
24 D. Ozhava and S. Ozkar, *Appl. Catal., B*, 2018, **237**, 1012–1020.
25 D. Özhava and S. Özkar, *Appl. Catal., B*, 2016, **181**, 716–726.
26 X. Y. Huang, Y. Y. Liu, H. Wen, R. F. Shen, S. Mehdi, X. L. Wu, E. J. Liang, X. J. Guo and B. J. Li, *Appl. Catal., B*, 2021, **287**, 119960.
27 H. Can and Ö. Metin, *Appl. Catal., B*, 2012, **125**, 304–310.
28 J. Manna, S. Akbayrak and S. Ozkar, *Appl. Catal., B*, 2017, **208**, 104–115.
29 S. Akbayrak, G. Çakmak, T. Öztürk and S. Özkar, *Int. J. Hydrogen Energy*, 2021, **46**, 13548–13560.
30 Y. Y. Liu, G. S. Han, X. Y. Zhang, C. C. Xing, C. X. Du, H. Q. Cao and B. J. Li, *Nano Res.*, 2017, **10**, 3035–3048.
31 S. Akbayrak and S. Ozkar, *J. Colloid Interface Sci.*, 2021, **596**, 100–107.
32 C. C. Cui, Y. Y. Liu, S. Mehdi, H. Wen, B. J. Zhou, J. P. Li and B. J. Li, *Appl. Catal., B*, 2020, **265**, 118612.
33 S. Chen, B. B. Gong, J. Gu, Y. Lin, B. Yang, Q. Q. Gu, R. Jin, Q. Liu, W. X. Ying, X. X. Shi, W. L. Xu, L. H. Cai, Y. Li, Z. H. Sun, S. Q. Wei, W. H. Zhang and J. L. Lu, *Angew. Chem., Int. Ed.*, 2022, **61**, e202211919.
34 S. Akbayrak, Z. Ozcifci and A. Tabak, *J. Colloid Interface Sci.*, 2019, **546**, 324–332.
35 M. Chandra and Q. Xu, *J. Power Sources*, 2007, **168**, 135–142.
36 X. G. Li, C. L. Zhang, M. H. Luo, Q. L. Yao and Z. H. Lu, *Inorg. Chem. Front.*, 2020, **7**, 1298–1306.
37 M. A. Khalily, H. Eren, S. Akbayrak, H. H. Susapto, N. Biyikli, S. Ozkar and M. O. Guler, *Angew. Chem., Int. Ed.*, 2016, **55**, 12257–12261.
38 J. Yang, W. Z. Fu, C. Q. Chen, W. Y. Chen, W. G. Huang, R. O. Yang, Q. Q. Kong, B. Y. Zhang, J. X. Zhao, C. M. Chen, J. Luo, F. Yang, X. Z. Duan, Z. Jiang and Y. Qin, *ACS Catal.*, 2021, **11**, 4146–4156.
39 X. Zhao, Z. Q. Yang, W. J. Wang, Y. X. Li, X. H. Zhou and H. B. Zhang, *J. Mater. Chem. A*, 2020, **8**, 7171–7176.
40 J. J. Li, Q. Q. Guan, H. Wu, W. Liu, Y. Lin, Z. H. Sun, X. X. Ye, X. S. Zheng, H. B. Pan, J. F. Zhu, S. Chen, W. H. Zhang, S. Q. Wei and J. L. Lu, *J. Am. Chem. Soc.*, 2019, **141**, 14515–14519.
41 J. K. Zhang, W. Y. Chen, H. B. Ge, C. Q. Chen, W. J. Yan, Z. Gao, J. Gan, B. Y. Zhang, X. Z. Duan and Y. Qin, *Appl. Catal., B*, 2018, **235**, 256–263.
42 S. S. Acharyya, S. Ghosh, Y. Yoshida, T. Kaneko, T. Sasaki and Y. Iwasawa, *ACS Catal.*, 2021, **11**, 6698–6708.
43 M. Boronat and A. Corma, *ACS Catal.*, 2019, **9**, 1539–1548.
44 H. Shi, S. Eckstein, A. Vjunov, D. M. Camaioni and J. A. Lercher, *Nat. Commun.*, 2017, **8**, 15442.
45 Y. Li, Y. Fu, C. Lai, L. Qin, B. Li, S. Liu, H. Yi, F. Xu, L. Li, M. Zhang, M. Xu, C. Du and W. Chen, *Environ. Sci.: Nano*, 2021, **8**, 3067–3097.
46 S. Ghosh, S. S. Acharyya, Y. Yoshida, T. Kaneko, Y. Iwasawa and T. Sasaki, *ACS Appl. Mater. Interfaces*, 2022, **14**, 18464–18475.
47 R. F. Shen, Y. Y. Liu, H. Wen, X. L. Wu, G. S. Han, X. Z. Yue, S. Mehdi, T. Liu, H. Q. Cao, E. J. Liang and B. J. Li, *Small*, 2021, **18**, 2105588.
48 Y. C. Chai, W. X. Shang, W. J. Li, G. J. Wu, W. L. Dai, N. J. Guan and L. D. Li, *Adv. Sci.*, 2019, **6**, 1900299.
49 N. Wang, Q. M. Sun, T. J. Zhang, A. Mayoral, L. Li, X. Zhou, J. Xu, P. Zhang and J. H. Yu, *J. Am. Chem. Soc.*, 2021, **143**, 6905–6914.
50 M. Navlani-Garcia, K. Mori, Y. Kuwahara and H. Yamashita, *NPG Asia Mater.*, 2018, **10**, 277–292.
51 W. Y. Chen, W. Z. Fu, B. X. Chen, C. Peng, G. Qian, D. Chen, X. Z. Duan and X. G. Zhou, *J. Catal.*, 2020, **385**, 289–299.
52 Y. Y. Liu, H. Wen, D. J. Zhou, X. Y. Huang, X. L. Wu, J. C. Jiang, X. J. Guo and B. J. Li, *Appl. Catal., B*, 2021, **291**, 120094.
53 S. S. Duan, G. S. Han, Y. H. Su, X. Y. Zhang, Y. Y. Liu, X. L. Wu and B. J. Li, *Langmuir*, 2016, **32**, 6272–6281.
54 X. Cui, Y. Liu, G. Han, M. Cao, L. Han, B. Zhou, S. Mehdi, X. Wu, B. Li and J. Jiang, *Small*, 2021, **17**, 2101607.
55 G. Yang, S. Y. Guan, S. Mehdi, Y. P. Fan, B. Z. Liu and B. J. Li, *Green Energy Environ.*, 2021, **6**, 236–243.
56 X. L. Cui, H. Li, G. Q. Yu, M. Yuan, J. Yang, D. Xu, Y. M. Hou and Z. P. Dong, *Int. J. Hydrogen Energy*, 2017, **42**, 27055–27065.
57 W. Y. Chen, Z. J. Wang, X. Z. Duan, G. Qian, D. Chen and X. G. Zhou, *Chem. Eng. Sci.*, 2018, **192**, 1242–1251.
58 W. Y. Chen, S. M. Chen, G. Qian, L. Song, D. Chen, X. G. Zhou and X. Z. Duan, *J. Catal.*, 2020, **389**, 492–501.
59 X. M. Ning, Y. H. Li, B. Q. Dong, H. J. Wang, H. Yu, F. Peng and Y. H. Yang, *J. Catal.*, 2017, **348**, 100–109.
60 G. Han, M. Hu, Y. Liu, J. Gao, L. Han, S. Lu, H. Cao, X. Wu and B. Li, *J. Solid State Chem.*, 2019, **274**, 207–214.
61 H. Lv, R. Wei, X. W. Guo, L. Z. Sun and B. Liu, *J. Phys. Chem. Lett.*, 2021, **12**, 696–703.
62 Q. L. Yao, K. Yang, X. L. Hong, X. S. Chen and Z. H. Lu, *Catal. Sci. Technol.*, 2018, **8**, 870–877.
63 C. L. Wang, Q. Wang, F. Y. Fu and D. Astruc, *Acc. Chem. Res.*, 2020, **53**, 2483–2493.
64 N. X. Kang, R. Djeda, Q. Wang, F. Y. Fu, J. Ruiz, J. L. Pozzo and D. Astruc, *Chemcatchem*, 2019, **11**, 2341–2349.

65 S. Y. Guan, L. L. An, S. Ashraf, L. N. Zhang, B. Z. Liu, Y. P. Fan and B. J. Li, *Appl. Catal., B*, 2020, **269**, 118775.
66 L. B. Wang, H. L. Li, W. B. Zhang, X. Zhao, J. X. Qiu, A. Li, X. S. Zheng, Z. P. Hu, R. Si and J. Zeng, *Angew. Chem., Int. Ed.*, 2017, **56**, 4712–4718.
67 F. Y. Fu, C. L. Wang, Q. Wang, A. M. Martinez-Villacorta, A. Escobar, H. B. Chong, X. Wang, S. Moya, L. Salmon, E. Fouquet, J. Ruiz and D. Astruc, *J. Am. Chem. Soc.*, 2018, **140**, 10034–10042.